Journal of Hydrospace Technology, Vol. 2 No. 2, 1996, pp. 1-13

A Computational Study on Turbulent Flow Characteristics around Full-form Tankers

Suak-Ho Van * and Hyoung-Tae Kim †

Abstract

This paper presents the result of a computational study on the wake characteristics of two tanker models, i.e. HSVA and Mystery hull forms. The focus of the study is on the distributions of axial, radial and tangential velocities of the two hull forms in way of the propeller, especially over the propeller disk. The effect of bilge vortices on the velocity distribution is also concerned. For the computation of stern and wake flows of the two hull forms, the incompressible Reynolds-Averaged Navier-Stokes(RANS) equations are numerically solved by the second order finite difference method, which employs a four stage Runge-Kutta scheme with a residual averaging technique and the Baldwin-Lomax model. The calculated pressure distributions on the hull surface and the axial, radial and tangential velocity distributions over the propeller disk are presented for the two hull forms. Finally, the result of wake analysis for the computed wake distribution over the propeller disk is given in comparison with those for the experimental wake distribution for the both hull forms.

1 Introduction

The calculations of the viscous flows around the HSVA and Mystery hull forms are carried out. An explicit finite difference method for the solution of the three-dimensional incompressible Reynolds-Averaged Navier-Stokes equations is used for the calculations. The method employs second order finite differences for the spatial discretization and a hybrid four stage time-stepping scheme for the numerical integration in time. In order to increase the time step, residual averaging scheme of Jameson[1] is adopted. For the turbulence closure, the Baldwin-Lomax model is exploited. To obtain the pressure field, the pressure-Poisson equation derived from the continuity equation in conjunction with the momentum equations, is iteratively solved with the appropriate Neumann boundary condition, which ensures the divergence-free velocity field. The nonstaggered grid system is chosen and a specific scheme for the discretization of the pressure-Poisson equation is introduced to suppress the pressure oscillations[2, 3]. A two-dimensional body-fitted grid is generated at each transverse section by using the 2D GRAPE method, which exploits an elliptic grid generation technique. The axial velocity and vorticity contours for the selected stations, the

*Member, Korea Research Institute of Ships and Ocean Engineering
†Member, Chungnam National University

pressure contours and limiting streamlines on the hull surface are also presented.
Also the axial velocity contours and transverse velocity vectors over the propeller disk are presented in comparison with available experimental data. The results of harmonic analysis for the calculated velocity components are also given and compared with those for the measured velocity data.

2 Governing equations and numerical method

2.1 Governing equations

The governing equations are the incompressible Reynolds-Averaged Navier-Stokes equations which describe the conservation of mass and momentum. The Reynolds-Averaged Navier-Stokes equations can be written in cylindrical polar coordinate with the primitive variables as follows.

$$\frac{\partial u}{\partial x}+\frac{1}{r}\frac{\partial}{\partial r}(rv)+\frac{1}{r}\frac{\partial w}{\partial \theta}=0, \tag{1}$$

$$\frac{\partial u}{\partial t}+u\frac{\partial u}{\partial x}+v\frac{\partial u}{\partial r}+\frac{w}{r}\frac{\partial u}{\partial \theta}=\frac{\partial P}{\partial x}+\frac{\partial \tau_{xx}}{\partial x}+\frac{1}{r}\frac{\partial(r\tau_{xr})}{\partial r}+\frac{1}{r}\frac{\partial \tau_{x\theta}}{\partial \theta}, \tag{2}$$

$$\frac{\partial v}{\partial t}+u\frac{\partial v}{\partial x}+v\frac{\partial v}{\partial r}+\frac{w}{r}\frac{\partial v}{\partial \theta}-\frac{w^2}{r}=\frac{\partial P}{\partial r}+\frac{\partial \tau_{xr}}{\partial x}+\frac{1}{r}\frac{\partial(r\tau_{rr})}{\partial r}+\frac{1}{r}\frac{\partial \tau_{r\theta}}{\partial \theta}-\frac{\tau_{\theta\theta}}{r}, \tag{3}$$

$$\frac{\partial w}{\partial t}+u\frac{\partial w}{\partial x}+v\frac{\partial w}{\partial r}+\frac{w}{r}\frac{\partial w}{\partial \theta}-\frac{vw}{r}=\frac{\partial P}{\partial \theta}+\frac{\partial \tau_{x\theta}}{\partial x}+\frac{1}{r}\frac{\partial(r\tau_{r\theta})}{\partial r}+\frac{1}{r}\frac{\partial \tau_{\theta\theta}}{\partial \theta}-\frac{\tau_{r\theta}}{r}. \tag{4}$$

All the variables are nondimensionalized by the speed of a ship V_S, the ship length L, fluid density ρ and viscosity μ. u, v, w represents the velocity components in axial, radial and tangential directions, respectively, P the static pressure and τ's are the total stresses including both viscous and Reynolds stresses.

For the computation of viscous flows around the hull forms of complex geometry, the governing equations in the cylindrical coordinates are transformed to general, curvilinear, body-fitted coordinates.

$$J[\frac{\partial}{\partial \xi}(\frac{U}{J})+\frac{\partial}{\partial \eta}(\frac{V}{J})+\frac{\partial}{\partial \zeta}(\frac{W}{J})]=0, \tag{5}$$

$$\frac{\partial Q}{\partial t}+A\frac{\partial Q}{\partial \xi}+B\frac{\partial Q}{\partial \eta}+C\frac{\partial Q}{\partial \zeta}+H-J(\frac{\partial E_{v1}}{\partial x}+\frac{\partial E_{v2}}{\partial \eta}+\frac{\partial E_{v3}}{\partial \zeta})-H_v=0. \tag{6}$$

where $J(=\frac{\partial(\xi,\eta,\zeta)}{\partial(x,r,\theta)})$ represents the Jacobian of transformation.

Q is the velocity vector defined as follows:

$$Q = (u, v, w)^T. \tag{7}$$

A, B, C are the diagonal matrices written respectively as follows,

$$A = diag(U, U, U),\ B = diag(V, V, V),\ C = diag(W, W, W), \tag{8}$$

where U, V, W are the contravariant velocity components respectively in ξ, η, ζ directions and written as follows;

$$U^i = u\xi^i_x + v\xi^i_r + \frac{w}{r}\xi^i_\theta, \quad \text{for } i = 1, 2, 3. \tag{9}$$

E_{v1}, E_{v2}, E_{v3} in equation(6) are the viscous flux vectors defined as follows;

$$E_{vj} = \frac{\nu_t}{J} \times \begin{bmatrix} (\xi_x\xi^j_x + g^{1j})u_\xi + (\eta_x\xi^j_x + g^{2j})u_\eta + (\zeta_x\xi^j_x + g^{3j})u_\zeta + S_{1j} \\ (\xi_r\xi^j_r + g^{1j})v_\xi + (\eta_r\xi^j_r + g^{2j})v_\eta + (\zeta_r\xi^j_r + g^{3j})v_\zeta + S_{2j} \\ (\frac{1}{r^2}\xi_\theta\xi^j_\theta + g^{1j})w_\xi + (\frac{1}{r^2}\eta_\theta\xi^j_\theta + g^{2j})w_\eta + (\frac{1}{r^2}\zeta_\theta\xi^j_\theta + g^{3j})w_\zeta + S_{3j} \end{bmatrix} \tag{10}$$

$$\text{for } j = 1, 2, 3,$$

where

$$\begin{aligned} S_{1j} &= \xi^j_r R_{21} + \frac{1}{r}\xi^j_\theta R_{31}, \\ S_{2j} &= \xi^j_x R_{12} + \frac{1}{r}\xi^j_\theta (R_{32} - \frac{w}{r}), \\ S_{3j} &= \frac{1}{r}(\xi^j_x R_{13} + \xi^j_r R_{23}) + \frac{1}{r}(\frac{2v}{r}\xi^j_\theta - w\xi^j_r), \end{aligned} \tag{11}$$

$$R_{ij} = u^i_\xi \xi_{xj} + u^i_\eta \eta_{xj} + u^i_\zeta \zeta_{xj}, \quad \text{for } i, j = 1, 2, 3, \tag{12}$$

$$(u^1, u^2, u^3) = (u, v, w), \qquad (x_1, x_2, x_3) = (x, r, \theta).$$

H and H_v in equation (6) are source vectors and can be written as follows;

$$H = \begin{bmatrix} \xi_x P_\xi + \eta_x P_\eta + \zeta_x P_\zeta \\ \xi_r P_\xi + \eta_r P_\eta + \zeta_r P_\zeta - \frac{w^2}{r} \\ \frac{1}{r}(\xi_\theta P_\xi + \eta_\theta P_\eta + \zeta_\theta P_\zeta + wv) \end{bmatrix} \tag{13}$$

$$H_v = \begin{bmatrix} 0 \\ -\frac{2\nu_t}{r}(R_{33} + \frac{v}{r}) \\ \frac{\nu_t}{r}(R_{23} + R_{32} - \frac{w}{r}) \end{bmatrix} \tag{14}$$

2.2 Discretization

For the discretization of spatial derivatives, the 3-point central differencing is used for pressure and viscous terms and the 2nd order upwind differencing is used for the convection terms. For the numerical integration of discretized momentum equations in time, 4-stage time-stepping scheme of Jameson is used. Applying these on Equations (5) and (6), following equations are obtained.

$$\nabla[Q^l_{i,j,k}] = 0, \quad \text{for } l = 1, 2, 3, 4, \tag{15}$$

$$Q^l_{i,j,k} = Q^n_{i,j,k} - \alpha_l \Delta t_{i,j,k} (RHS)^{l-1}_{i,j,k}, \quad \text{for } l = 1, 2, 3, 4. \tag{16}$$

Superscript n denotes the previous time step, l the intermediate or iteration time level between n and $n+1$ time step. In case of 4-stage scheme, $\alpha_1 = \frac{1}{4}, \alpha_2 = \frac{1}{3}, \alpha_3 = \frac{1}{2}, \alpha_4 = 1$ and RHS denotes the discretized form of the momentum equation (6) except the time derivative term. $\Delta t_{i,j,k}$ represents the time increment at (i, j, k) grid point.

The discretized pressure-Poisson equation used in the calculation can be written as follows;

$$(1-\epsilon)L[P^{l-1}_{i,j,k}] + \epsilon \tilde{L}[P^{l-1}_{i,j,k}] + N[P^{l-1}_{i,j,k}] = \frac{1}{\alpha_l}\nabla[Q^n_{i,j,k}] - \sigma^{l-1}_{i,j,k}. \tag{17}$$

The operators $(L, \tilde{L}, N)$ and source function(σ) are defined as follows;

$$L[P_{i,j,k}] = [\delta_\xi(\frac{g^{11}\Delta t}{J}\delta_\xi) + \delta_\eta(\frac{g^{22}\Delta t}{J}\delta_\eta) + \delta_\zeta(\frac{g^{33}\Delta t}{J}\delta_\zeta)][P_{i,j,k}], \tag{18}$$

$$\tilde{L}[P_{i,j,k}] = [\tilde{\delta}_\xi(\frac{g^{11}\Delta t}{J}\delta_\xi) + \tilde{\delta}_\eta(\frac{g^{22}\Delta t}{J}\delta_\eta) + \tilde{\delta}_\zeta(\frac{g^{33}\Delta t}{J}\delta_\zeta)][P_{i,j,k}], \tag{19}$$

$$\begin{aligned} N[P_{i,j,k}] &= \{\delta_\xi[\frac{\Delta t}{J}(g^{12}\delta_\eta + g^{13}\delta_\zeta)] \\ &+ \delta_\eta[\frac{\Delta t}{J}(g^{12}\delta_\xi + g^{23}\delta_\zeta)] \\ &+ \delta_\zeta[\frac{\Delta t}{J}(g^{13}\delta_\xi + g^{23}\delta_\eta)]\}[P_{i,j,k}], \end{aligned} \tag{20}$$

$$\begin{aligned}\sigma_{i,j,k} &= \delta_\xi[\frac{\Delta t}{J}(\xi_x f^x + \eta_x f^r + \zeta_x f^\theta)]_{i,j,k} \\ &+ \delta_\eta[\frac{\Delta t}{J}(\xi_r f^x + \eta_r f^r + \zeta_r f^\theta)]_{i,j,k} \\ &+ \delta_\zeta[\frac{\Delta t}{rJ}(\xi_\theta f^x + \eta_\theta f^r + \zeta_\theta f^\theta)]_{i,j,k}.\end{aligned} \tag{21}$$

2.3 Grids generation and boundary conditions

A body-fitted grid is generated by using the elliptic grid generation technique at each transverse section of ξ = constant as shown in Figures 1a &1b. $115 \times 41 \times 33$ grids are used in axial, radial and tangential directions, respectively. Inlet boundary is located at $0.5L$ in front of FP ($\xi = -0.976$), exit boundary at $\xi = 1.5$ and outer boundary at $0.5L$ from the centerline of a ship in radial direction.
As the inlet boundary condition, uniform flow ($U = 1, V = W = 0$) for velocity and Neumann condition for pressure is applied. $U_{\xi\xi} = V_{\xi\xi} = W_{\xi\xi} = 0$ and $P_\xi = 0$ is applied on the exit boundary, $U_{\eta\eta} = V_{\eta\eta} = W_{\eta\eta} = 0$ and $P_\eta = 0$ on the outer boundary, symmetry condition ($U_\theta = V_\theta = W_\theta = P_\theta = 0$) on the centerplane in front and behind of a ship and waterplane, non-slip boundary condition ($U = V = W = 0$) and Neumann condition for the pressure on the hull surface.

3 Computational Results

Numerical calculations are performed for two tanker models, one is known as an HSVA tanker(also known as a Hoffman Tanker) and the other one is known as Mystery hull form. Flow characteristics between two hull forms are compared based on the computational results, especially the pressure distribution on the hull surface, velocity and axial vorticity distributions at selected transverse sections and the limiting streamlines on the hull surface. Also the results of wake analysis of the velocity distributions in the propeller plane are shown and compared with those of experiments.

3.1 General Features of Hull Forms

The fore part of two hull forms are exactly the same from FP to midship and after part of Mystery hull is modified as moderate U-type from that of HSVA tanker which can be considered as V-type. In the 1990 SSPA-CTH-IIHR workshop on the 'Ship Viscous Flow'[4], the attendants were asked to present the computational results of those two hull forms, and the organizer wanted to see whether the computational results can grasp the different flow characteristics as shown in experiments or not. The body plans of the hull forms are compared in Figures 2a & 2b. The latter hull form is designed to make the velocity distribution at the propeller plane more uniform, thus improving the propulsion and cavitation characteristics of the propeller. The velocity contour lines of the HSVA

tanker are relatively straight, on the other hand, those of the Mystery Hull are much more curved, indicating more uniform inflow to the propeller[5]. This is because the longitudinal vortices formed at the bilge of the U-shaped stern are much stronger than those of the V-shaped stern as shown by Dyne based on the experiments.

3.2 Pressure Distributions on Hull Surface

As expected from the geometry of two hull form, the pressure distributions on the front parts of both hull form are exactly the same as shown in Figure 3. On the middle part, there are small differences of the pressure maybe due to the influence from the difference of the stern parts. Near the bilge of the stern part, the surface pressure of the Mystery hull is lower than that of the HSVA hull and the pressure recovery at the stern is slightly slower for the Mystery than the HSVA hull. This indicates a larger pressure resistance of the Mystery hull compared to that of the HSVA hull. It could be also related with a stronger longitudinal vortices formed in case of the former.

3.3 Axial Velocity and Vorticity Distributions

Axial velocity and vorticity distributions at the selected sections are shown in Figures 4 and 5, respectively. In general, the axial velocity contours show very well the development of the ship boundary layer and thick stern boundary layer. Although the differences of the axial velocity contours between both hull forms are relatively small over the whole ship length, the overall area of the viscous shear region is little larger for the Mystery hull than the HSVA hull, which is considered to be consistent with the larger resistance coefficient of the former than the latter.

The axial vorticity distributions of both hull forms are quite similar, but the strength of the vorticity is much larger in the case of the Mystery hull than that of the HSVA, especially near the stern part. In addition, the cores of the longitudinal vortices generally match with the lowest axial momentum regions in both cases.

3.4 Limiting Streamlines on Hull Surfaces

The calculated limiting streamlines on the surfaces of two hull forms are shown in Figures 7a & 7b. For the HSVA model, there is a line of divergence along the keel, which bends down in vertical direction very near the stern and merges in a strong focus located at the bottom of the stern. There are also a saddle point, another weak focus and a vertical line of divergence goes up to the symmetry plane(water plane), which clearly displays the complexity of the ship stern flow including the three-dimensional separation. A small region of reversed flow is predicted between the strong focus and a saddle point which dividing the vertical lines of divergence. The overall characteristics of the limiting streamlines of the Mystery hull is analogous to that of the HSVA hull. However, the horizontal line of divergence bends up further and then down, which seems connected to a very weak focus and also to another line of divergence located near the bottom of the stern. Two vertical lines of divergence are clearly formed, which are separated by a saddle point. Compared to

the surface-flow pattern obtained from the paint tests, the main features are well captured by the present computation.

3.5 Resistance Components

The frictional resistance and viscous pressure resistance are calculated by integrating the wall shear stress and hull surface pressure. C_f, C_P and C_S(wetted surface area coefficient defined as $\frac{S}{2H+B}$)[6] are presented in Table 1 and compared with the C_f value calculated from 1957 ITTC model-ship correlation line for reference. Also the wetted surface area is compared with that of Collatz to check the accuracy of the hull form presentation and integration. The C_f values for both hulls are almost same for both hulls but small compared to the value from ITTC line. The reason for the differences are not clear at present time but the insufficiency of the grid resolution and inadequacy of the turbulence model used in this computation might be the parts of it. C_P of Mystery hull is slightly larger than that of HSVA hull as expected, but the difference is too small to be compared quantitatively.

	HSVA	Mystery
$C_f \times 10^3$ (Cal.)	2.894	2.872
$C_P \times 10^3$ (Cal.)	0.420	0.430
$C_f \times 10^3$ (ITTC)	3.397	3.397
C_S (Cal.)	0.8843	0.8841
C_S (Collatz)	0.8815	–

3.6 Wake Analysis

Figures 8a, 8b, 8c & 8d show the experimental and computational velocity distributions over the propeller disk for the HSVA and Mystery tanker models, respectively. In order to obtain the computed velocity distribution over the propeller disk, first a simple linear interpolation of each velocity component and grid coordinate is done in axial direction and then a bilinear interpolation using isoparametric mapping is applied for the velocity components at the cobwebby grid points fitted to the propeller disk. The same bilinear interpolation is also applied to the measured velocities to get those at the same grid points over the propeller disk. Although the different wake characteristics due to the stern shapes of the two hull forms are shown successfully, the computed velocity distributions does not show a good agreement with the experimental data enough for the practical use. Part of the disagreement could stem from the difference in the stern shape used in the calculation and the experiments very close to the propeller disk. The deficiency of the Baldwin-Lomax turbulence model could also be an another reason to cause the disagreement.

In Figures 9 and 10, the results of the harmonic analyzes for the axial, radial and tangential components of velocity distributions obtained from the computations and the experiments over the propeller disk are compared for the HSVA and Mystery tanker models, respectively. The computed harmonics show the general trend of those of the experiments.

Finally, the radial distribution of the circumferentially averaged axial velocity components over the propeller disk is given in Figure 11. The calculated distribution for the HSVA

tanker model agrees rather well with the experimental result, except the region very near the propeller bossing, the geometry of which were not correctly included in the calculation. However, the result for the Mystery tanker model shows the same trend but higher velocity over the propeller disk compared with the experiments.

4 Summary

Viscous flow around two tankers, one is HSVA tanker and the other Mystery hull are solved numerically. The axial velocity and vorticity contours for the selected stations, the pressure contours and limiting streamlines on the hull surface obtained from the computational results are presented and compared between two hull forms.
The differences of the flow characteristics around the stern of two hull forms are predicted well in general, but the resistance components integrated from the shear stress and pressure are slightly less than those expected. The general trends of wake characteristics due to the stern shapes of two hull forms are well captured in the computation but quantitatively the results are not fully satisfactory when compared with those of experiments. Further study to increase the accuracy of the computation is necessary and also to analyze the flow obtained from the computation.

Acknowledgement

This paper is based on the results from a Advanced Research Program (ND323) of KRISO, supported by the Ministry of Science and Technology. The CRAY-C90 Supercomputer of System Engineering Research Institute(SERI) is used for the computations in this paper.

References

[1] Jameson, A. and Schmidt, W., "Some Recent Developments in Numerical Methods for Transonic Flows," *Computer Methods in Applied Mech. and Eng.*, 51, 1985.

[2] Van, S.H. and Kim, H.T., "Computation of Turbulent Flow around Wigley Hull Using 4-Stage Runge-Kutta Scheme on Nonstaggered Grid," *Transactions of the Society of Naval Architects of Korea,* Vol. 31, No. 3, Aug., 1994

[3] Sotiropoulos, F., "A Primitive Variable Method for the Solution of External and Internal Incompressible Flow- Fields,", Ph.D. Thesis, the Univ. of Cincinnati, Cincinnati, OH, 1991.

[4] "Ship Viscous Flow," *Prco. of 1990 SSPA-CTH-IIHR Workshop,* Flowtech International AB, Gothenburg, 1991.

[5] Dyne, G., "A Study of the Scale Effect on Wake, Propeller Cavitation, and Vibratory Pressure at Hull of Two Tanker Models," *Trans. of SNAME,* Vol. 82, 1974.

[6] Collatz, G., "Mass-stabsuntersuchungen für ein Modell grosser Völligkeit," Forschungszentrum des Deutschen Schiffbaus, Hamburg, Bericht Nr. 28, 1972

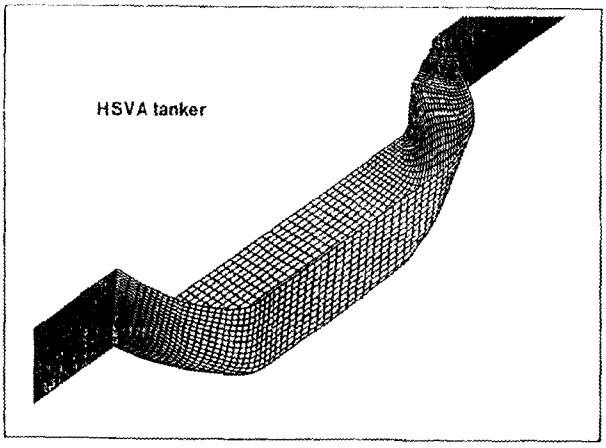

Fig. 1a Perspective view of computational grid(HSVA)

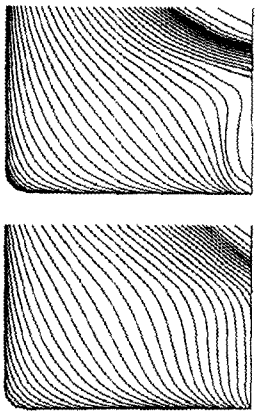

Fig. 2 Body plans of HSVA(top) and Mystery(bottom) hull forms

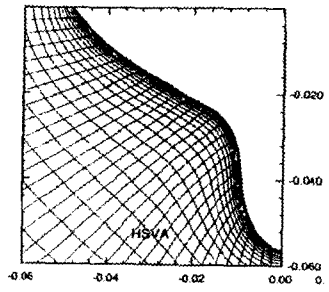

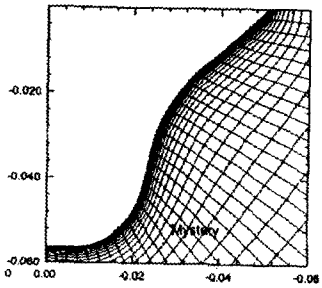

Fig. 1b Computational grid at typical transverse section

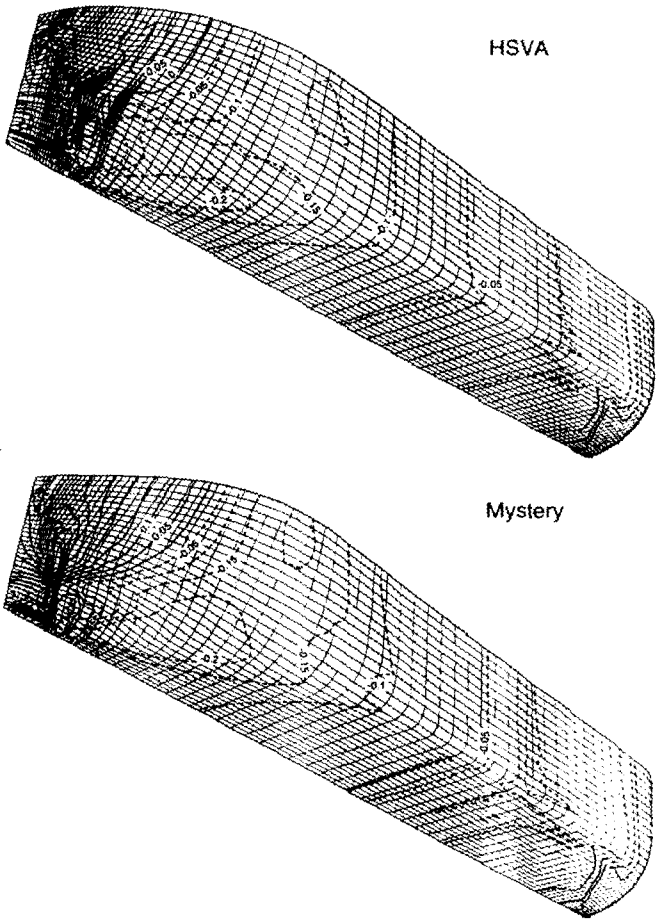

Fig. 3 Distribution of hull surface pressure

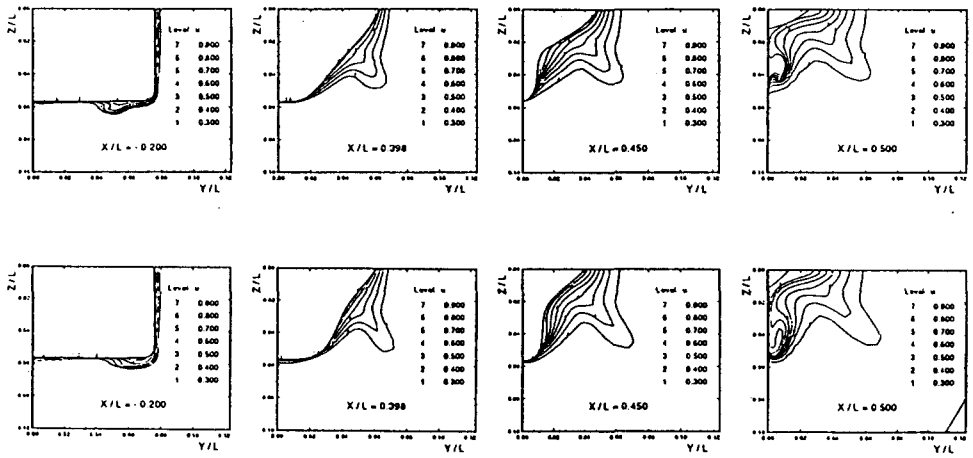

Fig. 4 Axial velocity contours(top:HSVA, bottom:Mystery)

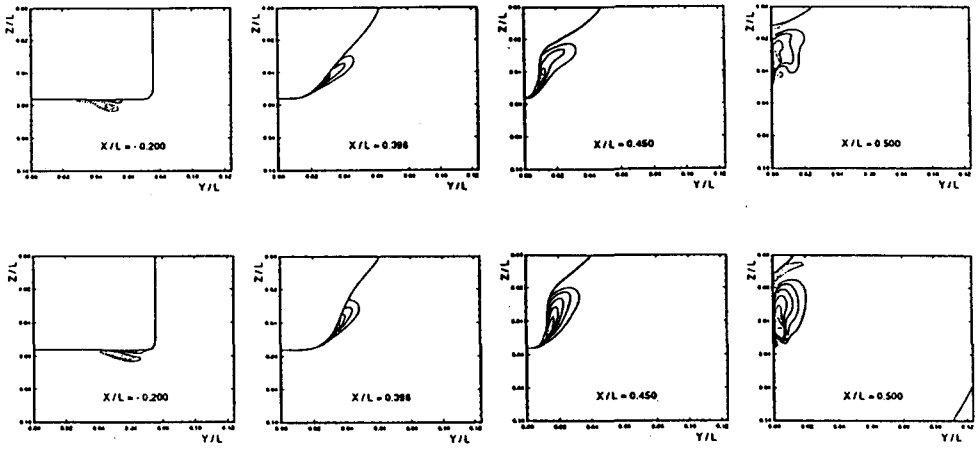

Fig. 5 Axial vorticity contours(top:HSVA, bottom:Mystery)

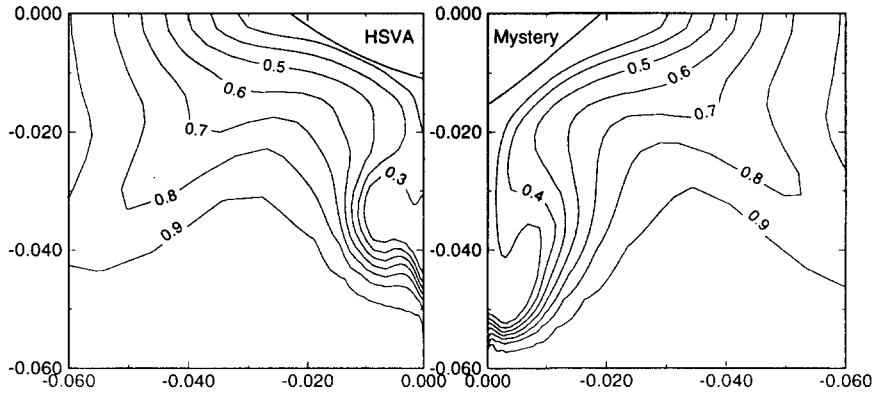

Fig. 6 Axial velocity distributions at propeller plane

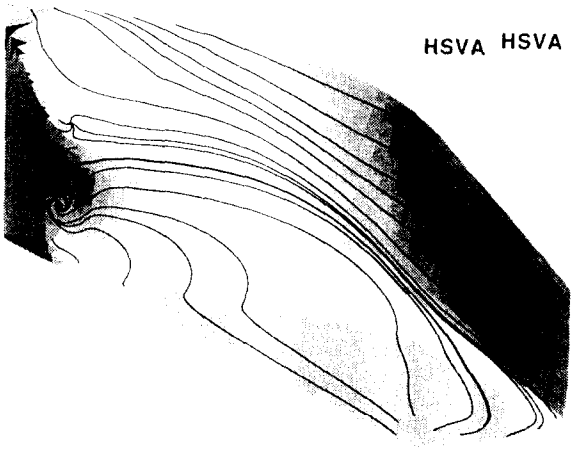

Fig. 7a Limiting streamlines(HSVA)

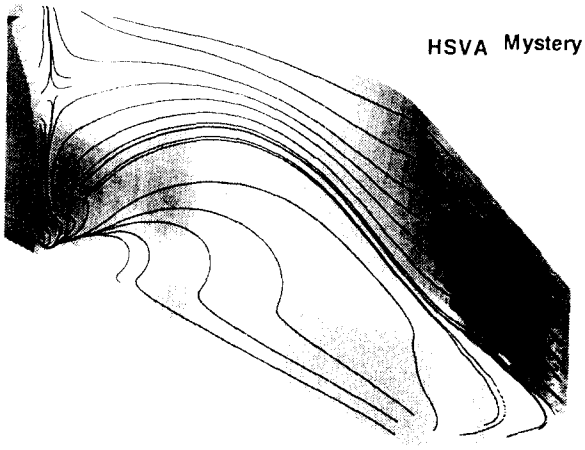

Fig. 7b Limiting streamlines(Mystery)

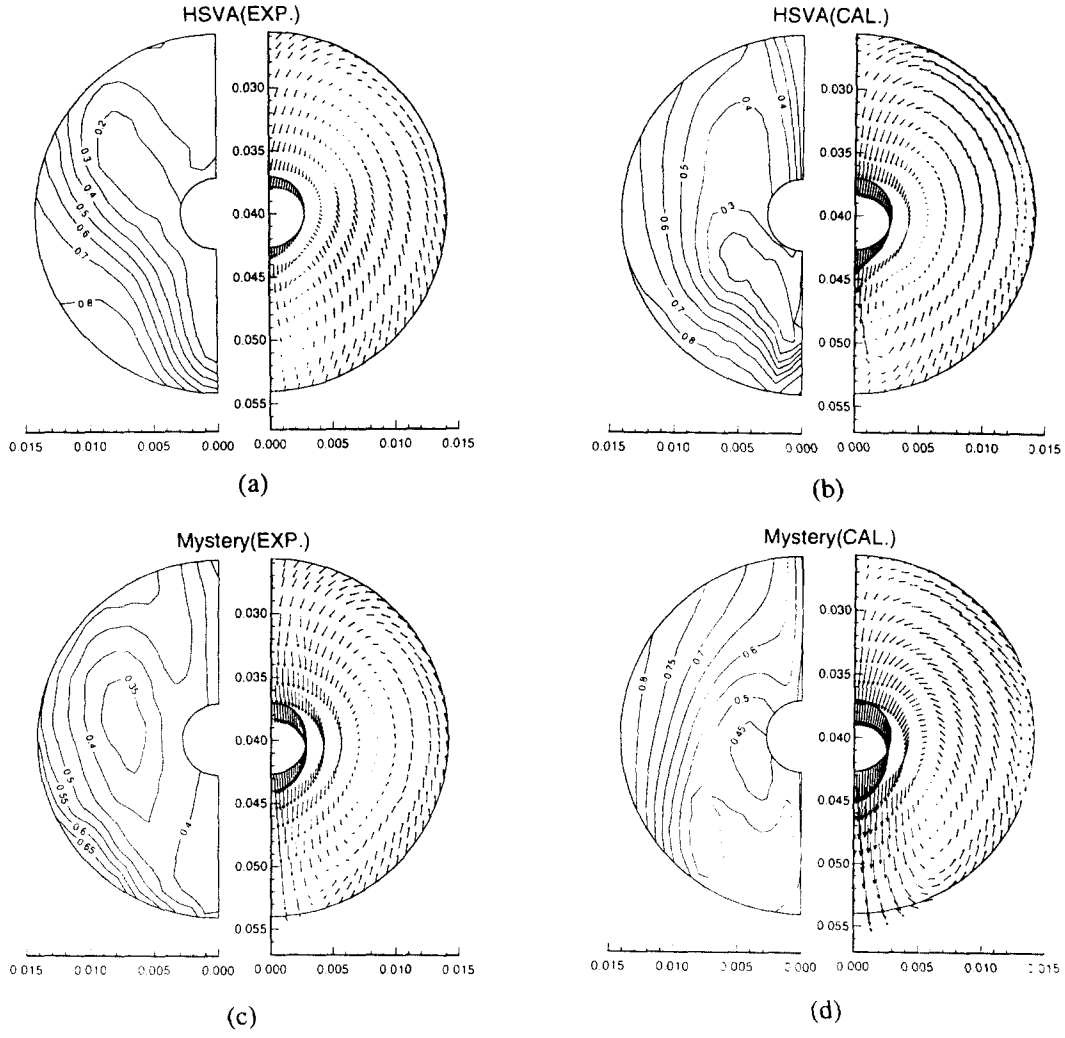

Fig. 8 Axial velocity contours & transverse vectors in propeller plane

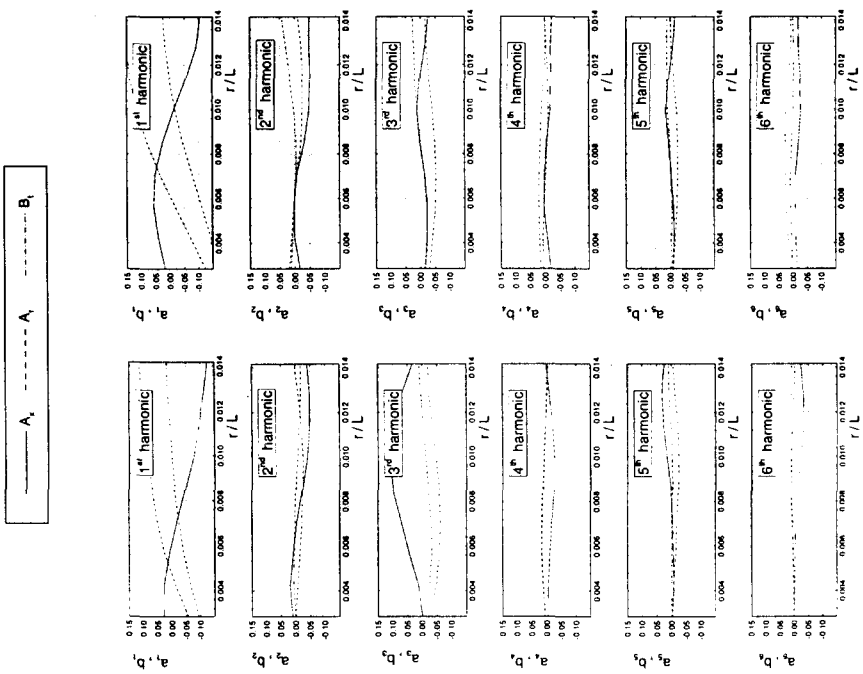

Fig. 9 Harmonic analysis of velocity components(HSVA)

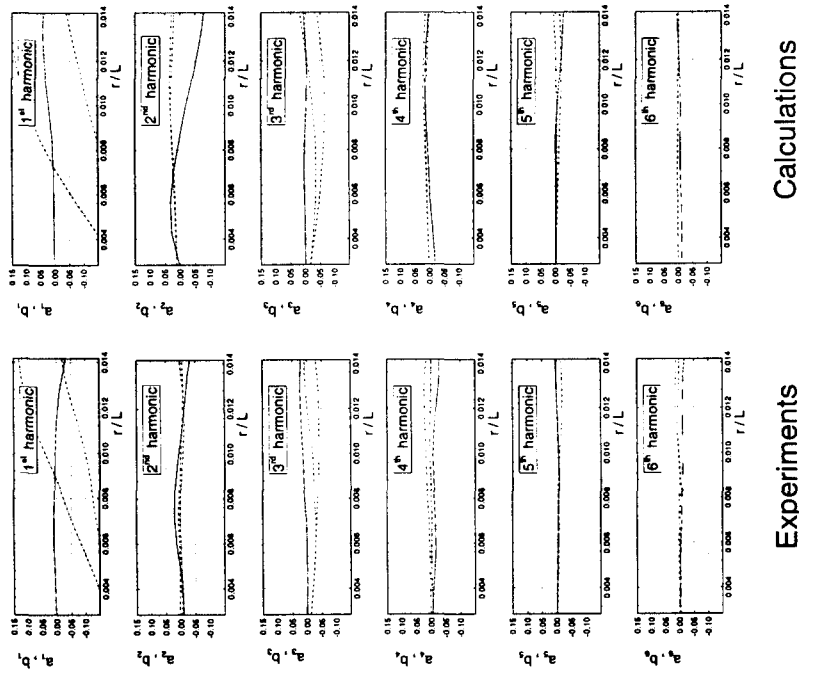

Fig. 10 Harmonic analysis of velocity components(Mystery)

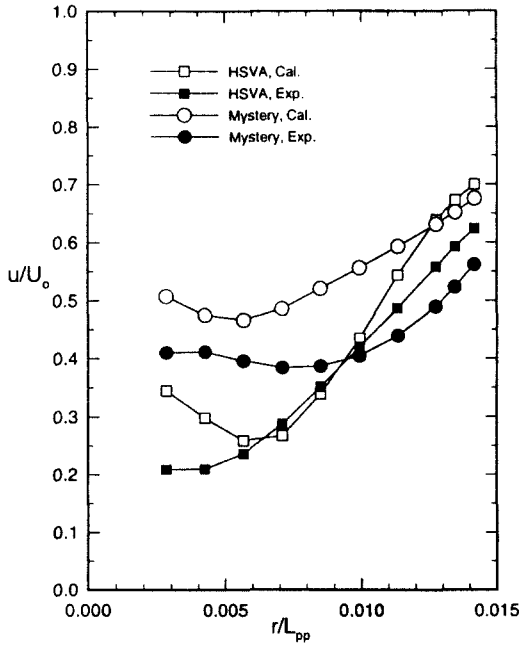

Fig. 11 Comparison of radial distribution of averaged axial velocity component